Article

Modulation of the morphotropic phase boundary for high-performance ductile thermoelectric materials

Jiasheng Liang[1,2,5], Jin Liu[1,2,5], Pengfei Qiu [1,2,3] ✉, Chen Ming [1], Zhengyang Zhou[1], Zhiqiang Gao[1,4], Kunpeng Zhao [4] ✉, Lidong Chen [1,2] & Xun Shi [1,2,4] ✉

The flexible thermoelectric technique, which can convert heat from the human body to electricity via the Seebeck effect, is expected to provide a peerless solution for the power supply of wearables. The recent discovery of ductile semiconductors has opened a new avenue for flexible thermoelectric technology, but their power factor and figure-of-merit values are still much lower than those of classic thermoelectric materials. Herein, we demonstrate the presence of morphotropic phase boundary in Ag_2Se-Ag_2S pseudobinary compounds. The morphotropic phase boundary can be freely tuned by adjusting the material thermal treatment processes. High-performance ductile thermoelectric materials with excellent power factor ($22\,\mu Wcm^{-1}K^{-2}$) and figure-of-merit (0.61) values are realized near the morphotropic phase boundary at 300 K. These materials perform better than all existing ductile inorganic semiconductors and organic materials. Furthermore, the in-plane flexible thermoelectric device based on these high-performance thermoelectric materials demonstrates a normalized maximum power density reaching $0.26\,Wm^{-1}$ under a temperature gradient of 20 K, which is at least two orders of magnitude higher than those of flexible organic thermoelectric devices. This work can greatly accelerate the development of flexible thermoelectric technology.

Flexible thermoelectrics can directly convert heat from the human body to electricity based on the Seebeck effect with the advantages of better portability, higher reliability, and longer lifetime than chemical batteries, making it a highly promising self-powered technology for wearable devices[1–4]. High-efficiency flexible thermoelectric (TE) technology requires materials with both high TE performance and good flexibility to adapt to curved body surfaces. The performance of a TE material can be evaluated by the dimensionless figure of merit

($zT = \alpha^2 \sigma T/\kappa$), where α is the Seebeck coefficient, σ is the electrical conductivity, κ is the thermal conductivity, and T is the absolute temperature[5–10]. In particular, high power factors ($PF = \alpha^2\sigma$) are essential for providing large output power under an assigned temperature difference (ΔT).

To achieve excellent flexibility, organic conducting polymers (e.g., PEDOT, P3HT, and PANI) are natural candidates for flexible thermoelectrics due to their inherent soft, bendable, and ductile

[1]State Key Laboratory of High Performance Ceramics and Superfine Microstructure, Shanghai Institute of Ceramics, Chinese Academy of Sciences, Shanghai, China. [2]Center of Materials Science and Optoelectronics Engineering, University of Chinese Academy of Sciences, Beijing, China. [3]School of Chemistry and Materials Science, Hangzhou Institute for Advanced Study, University of Chinese Academy of Sciences, Hangzhou, China. [4]State Key Laboratory of Metal Matrix Composites, School of Materials Science and Engineering, Shanghai Jiao Tong University, Shanghai, China. [5]These authors contributed equally: Jiasheng Liang, Jin Liu. ✉e-mail: qiupf@mail.sic.ac.cn; zkp.1989@sjtu.edu.cn; xshi@mail.sic.ac.cn

mechanical properties[11–13]. However, their carrier mobilities are extremely low (usually less than $1\,cm^2V^{-1}s^{-1}$), resulting in lower *PF* (usually less than $1\,\mu W\,cm^{-1}K^{-2}$) and *zT* values (usually less than 0.1) than classic brittle inorganic TE materials with high *PF* (higher than $20\,\mu W\,cm^{-1}K^{-2}$) and *zT* (approximately 0.8-1.0) values at room temperature[14,15]. The recently discovered ductile inorganic materials, such as Ag$_2$S-based compounds, are highly suitable for flexible thermoelectrics because they possess mechanical properties similar to those of organic polymers and high carrier mobilities similar to those of classic inorganic materials[1,16–19]. The former can lead to excellent flexibility, while the latter can result in high *PF* and *zT* values similar to those of inorganic TE materials. At room temperature, Ag$_2$S is ductile, but its *PF* and *zT* values are extremely low (negligible at 300 K)[17]. Alloying a certain amount of Se/Te in Ag$_2$S leads to the discovery of a series of n-type and p-type high-performance ductile inorganic TE materials with a maximum *PF* value of ~5 $\mu W\,cm^{-1}K^{-2}$ and a maximum *zT* value of ~0.45 at 300 K[1,17,19–28]. These numbers are superior to those of present organic TE materials[29–35], but they are still much lower than those of classic Bi$_2$Te$_3$- and Ag$_2$Se-based TE materials[14,15,36–38], greatly limiting the power output and applicability of flexible devices based on these ductile TE materials.

The morphotropic phase boundary (MPB) is a transition region in the oblique temperature–composition phase diagram that separates two competing phases with different crystallographic symmetries[39–43], such as the rhombohedral and tetragonal structures in lead zirconate titanate (PZT). The sharp extrema in piezoelectric properties near the MPB lead to unprecedented piezoelectric properties from both fundamental research and practical applications[39,40]. However, MPB has rarely been observed in TE materials due to the lack of material competing phases with distinct crystallographic symmetry and TE performance characteristics. In Ag₂(Se,S)-based compounds, the crystal structure changes from orthorhombic to monoclinic with increasing S content. This transformation indicates that an oblique temperature–composition phase boundary may exist. More importantly, both the mechanical ductility and TE performance are quite different between orthorhombic and monoclinic materials; that is, orthorhombic Ag$_2$Se is fragile and has a high *PF/zT* (*zT* reaching 1.0) at room temperature, while monoclinic Ag$_2$S is ductile and has a low *PF/zT* at room temperature[14,17,44]. All these features strongly indicate that MPBs similar to those in PZT-based compounds may exist in Ag₂(Se,S)-based compounds.

In this work, we demonstrate that the MPB separating orthorhombic and monoclinic structures is present in Ag$_2$Se-Ag$_2$S pseudobinary compounds. This boundary can be freely tuned by adjusting the thermal treatment process. The orthorhombic Ag$_2$Se$_{1-x}$S$_x$ pseudobinary compounds near the MPB effectively integrate the characteristics of excellent TE performance and good ductility, boosting the maximum room-temperature *PF* and *zT* values of ductile materials to $22\,\mu W\,cm^{-1}K^{-2}$ and 0.61, respectively (Fig. 1). Furthermore, based on these high-performance ductile TE materials, a fully flexible in-plane TE device is successfully developed with a superior normalized material exhibiting a maximum power density reaching $0.26\,W\,m^{-1}$ under a temperature gradient of 20 K.

Results and discussion

When the S content *x* is smaller than 0.2, Ag$_2$Se$_{1-x}$S$_x$ pseudobinary compounds have orthorhombic structures similar to those of Ag$_2$Se; when *x* is larger than 0.4, Ag$_2$Se$_{1-x}$S$_x$ pseudobinary compounds have monoclinic structures similar to those of Ag$_2$S (see the X-ray diffraction patterns obtained for bulk Ag$_2$Se$_{1-x}$S$_x$, Fig. S1)[45]. Accordingly, the mechanical and TE properties are determined by the crystal structures of the material. When $x \leq 0.2$, the materials are brittle with high *PF* and *zT* values similar to those of Ag$_2$Se; when $x \geq 0.4$, the materials are ductile with low *PF* and *zT* values similar to those of Ag$_2$S[44].

The case is quite different and complicated when the S content *x* is between 0.2 and 0.4. By taking Ag$_2$Se$_{0.61}$S$_{0.39}$ as an example, the heat flow curves measured by differential scanning calorimetry (DSC) are displayed in Fig. 2a and Fig. S2. Differing from the single endothermic peak observed in Ag$_2$S (monoclinic–cubic transition) and Ag$_2$Se (orthorhombic–cubic transition), there are two endothermic peaks from 300 K to 400 K in Ag$_2$Se$_{0.61}$S$_{0.39}$, indicating that there are two phase transitions. The powder X-ray diffraction patterns collected at different temperatures indicate that Ag$_2$Se$_{0.61}$S$_{0.39}$ crystalizes in an orthorhombic structure at 300 K, in a monoclinic structure at 350 K, and in a cubic structure at 400 K (Fig. 2b). The Rietveld refinement proves that the orthorhombic phase and monoclinic phase are both pure (Fig. S3 and Table S1). Thus, the two-phase transitions are an orthorhombic–monoclinic transition and a monoclinic–cubic transition. Furthermore, the phase transition temperatures determined by the measurements during the heating and cooling processes are obviously different, indicating strong thermal hysteresis.
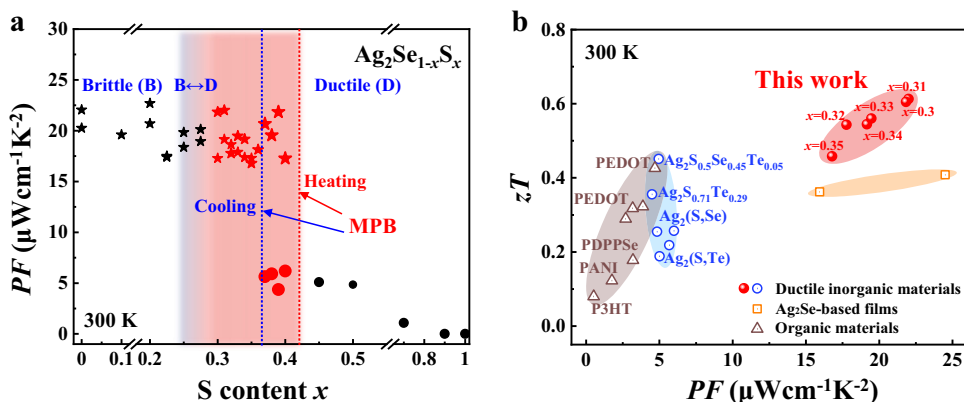
Fig. 1 | High-performance ductile Ag$_2$Se$_{1-x}$S$_x$ pseudobinary compounds.
a Room-temperature power factor (*PF*) as a function of *x* in Ag$_2$Se$_{1-x}$S$_x$ pseudobinary compounds. The dashed lines represent the orthorhombic–monoclinic morphotropic phase boundary (MPB) obtained during heating and cooling. The pentagrams represent orthorhombic structures, and the circles represent monoclinic structures. The red pentagrams and circles represent ductile Ag$_2$Se$_{1-x}$S$_x$ near

the MPB. **b** Room-temperature TE figure of merit (*zT*) as a function of *PF* for ductile orthorhombic Ag$_2$Se$_{1-x}$S$_x$ ($0.30 \leq x \leq 0.35$) pseudobinary compounds. Previously reported data about other typical ductile inorganic TE materials, organic TE materials, and Ag$_2$Se-based films are included for comparison. The data are taken from Refs. 1,17,19,20,22,29–38,44.
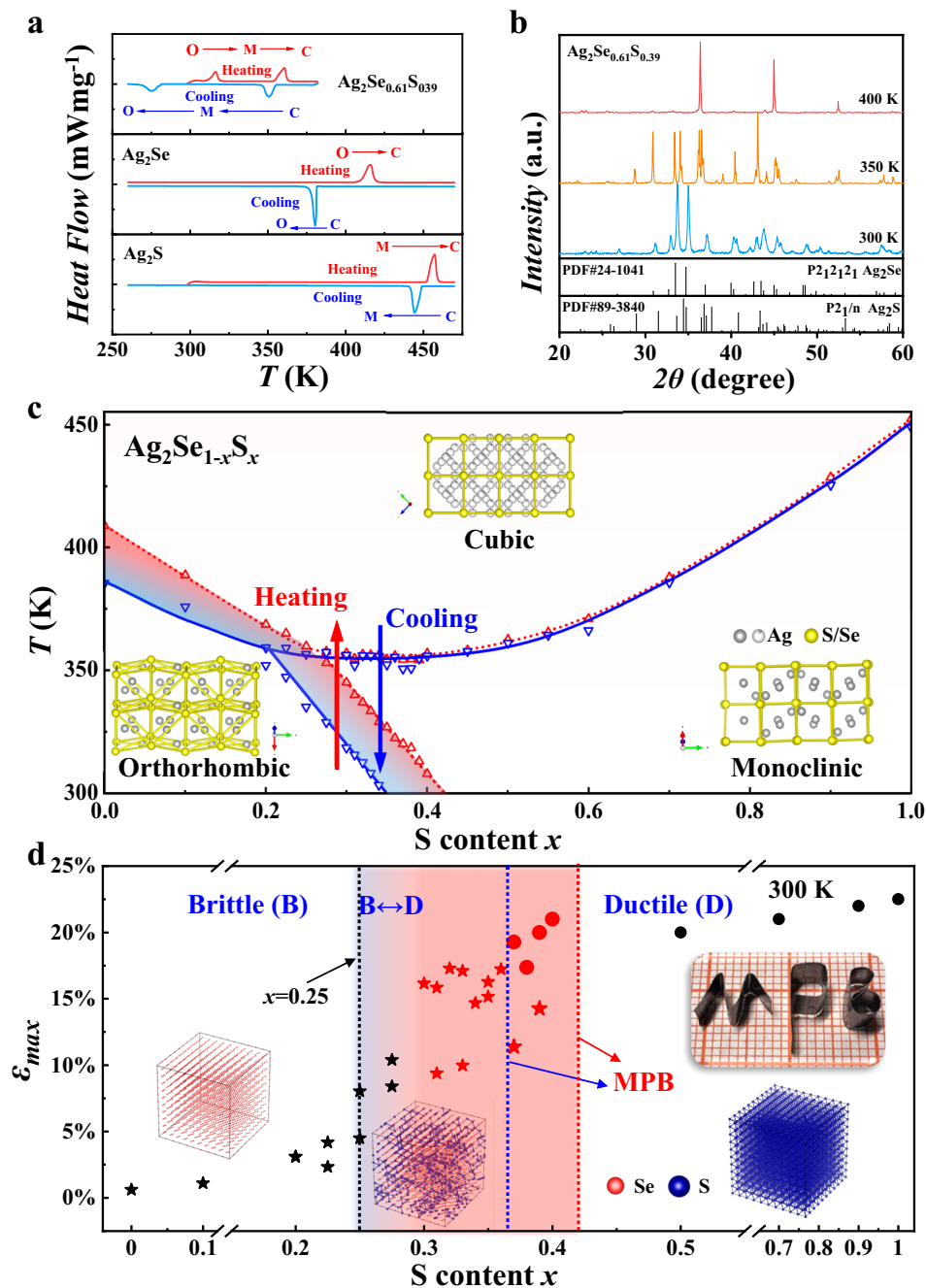
Fig. 2 | Phase transition and mechanical properties of $Ag_2Se_{1-x}S_x$ pseudobinary compounds. **a** Heat flow curves of $Ag_2Se_{0.61}S_{0.39}$ during heating and cooling processes. The letters O, M, and C represent orthorhombic, monoclinic, and cubic structures, respectively. **b** Powder X-ray diffraction patterns of $Ag_2Se_{0.61}S_{0.39}$ measured at different temperatures. The powders are ground in liquid nitrogen. **c** Ag_2Se-Ag_2S phase diagram between 250 and 480 K based on the heat flow curves shown in Fig. S2. The red and blue lines represent the phase boundaries in the heating and cooling processes, respectively. The triangles represent the experimental data. The insets in **c** are schematics of the cation Se/S framework in orthorhombic, monoclinic, and cubic structures. **d** Maximum bending strain (ε_{max}) as a function of x. ε_{max} is determined by the three-point bending test. The brittle–ductile boundary occurs at approximately $x = 0.25$–0.30. The upper right inset is an optical image of orthorhombic $Ag_2Se_{0.67}S_{0.33}$ twisted into different shapes. The bottom insets show the schematics of the percolation effect in three dimensions, with the percolation threshold occurring at approximately $x = 0.25$–0.31. The stars and circles represent orthorhombic and monoclinic $Ag_2Se_{1-x}S_x$, respectively. The red pentagrams and circles represent ductile $Ag_2Se_{1-x}S_x$ near the MPB.

By using the same method, a Ag_2Se-Ag_2S pseudobinary phase diagram between 300 and 480 K is obtained (see Fig. 2c). The red lines represent the phase boundaries in the heating process, while the blue lines represent the phase boundaries in the cooling process. When x is larger than 0.4, the phase transition temperatures (monoclinic–cubic transition) are almost the same between the heating and cooling processes. When x is smaller than 0.2, the phase transition temperatures of orthorhombic–cubic transitions in the cooling process are lower than those in the heating process. When x is 0.2–0.4, the phase transition temperatures of the orthorhombic–cubic transitions and orthorhombic–monoclinic transitions in the cooling process are lower than those in the heating process. This thermal hysteresis leads to different phase boundaries, as shown in Fig. 2c. By taking $Ag_2Se_{0.61}S_{0.39}$ as an example, the room-temperature structure is orthorhombic in the heating process and monoclinic in the cooling process (Fig. S4). Nevertheless, the orthorhombic–monoclinic transition temperature

gradually decreases with increasing x, resulting in oblique temperature–composition phase boundaries similar to those of the well-known MPB between the tetragonal and rhombohedral PZT phases[39,40]. The cubic $Ag_2Se_{1-x}S_x$ ($0.2 < x < 0.4$) pseudobinary compounds are first converted to a monoclinic structure and then converted to an orthorhombic structure in the cooling process; these results are reversed in the heating process.

These composition-induced orthorhombic–monoclinic transitions can be understood by the energy variations using first-principle calculations. The formation energies of the materials with orthorhombic structure (E_O) and monoclinic structure (E_M) are shown in Fig. S5. The differences (E_O–E_M) are 19.7 meV atom⁻¹ when $x=0$ and −27.1 meV atom⁻¹ when $x=1$, consistent with the scenario in which Ag_2S crystalizes in a monoclinic structure, while Ag_2Se crystalizes in an orthorhombic structure at room temperature. The difference ($E_O − E_M$) increases with increasing x, reaching zero when x is approximately 0.6 (Fig. S5). The structural competition between these two phases with nearly the same energies is responsible for the formation of MPB in the experimental phase diagram, as shown in Fig. 2c.

Interestingly, although the lattice symmetry of the orthorhombic structure is higher than that of the monoclinic structure, the cation Se/S framework in the cubic structure is more similar to that in the monoclinic structure (insets in Fig. 2c). In the monoclinic structure, the arrangement of Se/S atoms can be viewed as a distorted cubic body-centered lattice. Thus, in the monoclinic–cubic phase transition, the Se/S atoms move slightly by a small external driving force, which is consistent with the negligible thermal hysteresis shown in Fig. 2c. However, the arrangement of Se/S atoms in the orthorhombic structure is quite different from those in either the monoclinic structure or cubic structure. Thus, a higher external driving force is needed, yielding obvious thermal hysteresis (Fig. 2c).

Figure 2d presents a plot of the maximum bending strain (ε_{max}) as a function of S content x with detailed engineering stress–strain curves measured by three-point bending tests shown in Fig. S6. A clear brittle–ductile transition occurs at approximately $x = 0.25$–0.30. The thermal history of the material has a negligible effect on this transition. When x is smaller than this threshold, the materials are brittle. However, when x is larger than the threshold, the materials are ductile regardless of whether the structure is orthorhombic or monoclinic. As shown in Figs. S6c, d, the maximum bending and compressive strains of the ductile materials near the MPB (e.g., $Ag_2Se_{0.61}S_{0.39}$ and $Ag_2Se_{0.64}S_{0.36}$) are comparable with those of ductile polycrystalline Ag_2S-based materials[1,16,17,19]. These ductile materials in the MPB region can be machined into thin strips and bent and twisted into different complex shapes without cracking (upper right inset of Fig. 2d), showing good flexibility similar to organic materials. The ductility in Ag_2S and the brittleness in Ag_2Se are usually understood from the point of view of chemical bonds[16,18]. It is believed that the Ag-S bonds are multicentered and diffuse, which respond to the easy movement of dislocations and thus good ductility, while the Ag-Se bonds do not have such characteristics. For $Ag_2Se_{1-x}S_x$ pseudobinary compounds, the Ag-S bonds are isolated when x is small, resulting in brittle features. In contrast, when x is large, the Ag-S bonds are percolated, resulting in ductile features (schematics shown in the insets of Fig. 2d). According to the three-dimensional percolation model, the percolation threshold is estimated to be approximately 0.25–0.31[46], which is consistent with the brittle–ductile transition region shown in Fig. 2d.

In contrast to the mechanical properties, the TE properties of $Ag_2Se_{1-x}S_x$ pseudobinary compounds are sensitive to crystal structures instead of the S content. Figs. S7–9 plot the temperature dependences of TE properties for $Ag_2Se_{1-x}S_x$ pseudobinary compounds. Abrupt changes in TE properties are observed in the phase transition range, which originate from the strong electron and phonon scattering caused by critical fluctuations[47,48]. Before the orthorhombic–monoclinic phase transition, $\sigma$ has a weak temperature dependence (Fig. S7), while κ increases with increasing temperature, which originates from the increased contribution of electron thermal conductivity (κ_e) (Fig. S8). Figure 3a–d presents summaries of the room-temperature TE properties of $Ag_2Se_{1-x}S_x$ pseudobinary compounds as a function of S content. The data are listed in Table SII. At room temperature, the $Ag_2Se_{1-x}S_x$ samples crystalizing in the orthorhombic structure have large σ, PF, κ, and zT values, while those crystalizing in the monoclinic structure have low σ, PF, κ, and zT values. This phenomenon is more obvious in the MPB region. At the same chemical composition, the σ of $Ag_2Se_{1-x}S_x$ crystallized in the orthorhombic structure is 2–3 times larger than that in the monoclinic structure, resulting in higher PF (Fig. 1a) and zT (Fig. 3d) values. Likewise, Fig. S10 shows that the S content x in $Ag_2Se_{1-x}S_x$ has little influence on the carrier concentration (n) for the orthorhombic structure but has a large impact on n for the monoclinic structure.

The large divergence in TE properties between orthorhombic and monoclinic structures can be explained by the band edges of the material. The band structures of $Ag_2Se_{0.5}S_{0.5}$ specimens crystallized in orthorhombic and monoclinic structures are shown in Fig. S11a. Although the conduction band minimum (CBM) values of these two structures are mainly contributed by Ag-5s electrons, the CBM of the orthorhombic structure is more disperse than that of the monoclinic structure, leading to the small carrier effective mass (m^*) near the value (Table S1 and Fig. 3e). The m^* of $Ag_2Se_{0.5}S_{0.5}$ in the orthorhombic structure is 0.15 m_e, which is approximately 1/3 of that in the monoclinic structure. A similar phenomenon can be observed in Ag_2S and Ag_2Se (Fig. 3e and Fig. S11b, c). Although such a small m^* in the orthorhombic structure results in a lower α than that in the monoclinic structure (Fig. S12a), much larger carrier mobility μ_H values (Fig. 3f and Fig. S12b) are observed, which give rise to the higher σ, PF, and zT values observed in the orthorhombic structure.

The above results indicate that high-performance $Ag_2Se_{1-x}S_x$ pseudobinary ductile TE materials exist near the MPB region with detailed chemical compositions determined by the material's thermal history. Good ductility and high PF/zT can be simultaneously realized when x is 0.25–0.36 and 0.25–0.42 for the heating process and cooling process, respectively. Therefore, by adjusting the material chemical composition and thermal treatment process, the MPB in $Ag_2Se_{1-x}S_x$ pseudobinary compounds can be modulated for the needed mechanical and TE properties. The maximum PF values of ductile orthorhombic $Ag_2Se_{1-x}S_x$ pseudobinary compounds at room temperature reach 22 μWcm⁻¹K⁻², approximately four times that for monoclinic $Ag_2Se_{1-x}S_x$[17]. The maximum zT value at room temperature is 0.61, approximately two times that for monoclinic $Ag_2Se_{1-x}S_x$[17]. These PF and zT values are record-high values (Fig. 1b) compared with the reported organic materials and ductile inorganic TE materials[1,11,17,19–22,29–35,44,49,50]. The maximum PF is comparable to that of Ag_2Se-based inorganic–organic hybrid materials[36–38]. In addition, the ductile $Ag_2Se_{1-x}S_x$ materials show good performance stability between 300 K and 400 K and high reproducibility (Figs. S13 and S14).

To confirm the high TE performance in these ductile materials near the MPB region, a flexible in-plane TE device with 6 n/p couples is fabricated taking orthorhombic $Ag_2Se_{0.67}S_{0.33}$ thin strips as n-type legs and Pt–Rh wires as p-type legs (Fig. 4a, b). The thickness and length of these strips are approximately 0.1 mm and 20 mm, respectively. As shown in Fig. 4c, the device has a high material normalized power density of 0.26 Wm⁻¹ under a temperature gradient of 20 K, which is approximately three times that of the $Ag_2Se_{0.5}S_{0.5}$/Pt–Rh device (0.08 Wm⁻¹) and more than two orders of magnitude higher than those of organic TE devices under the same conditions[17,20,51–56] (Fig. 4c). Such a large value is contributed by the very high PF values of orthorhombic TE materials. Likewise, the excellent ductility of orthorhombic $Ag_2Se_{0.67}S_{0.33}$ promises the good flexibility of our device. At a bending radius of 7.5 mm, the internal resistance of the device is scarcely changed after 100 bending cycles (Fig. 4d), indicating high service durability in real-life applications.
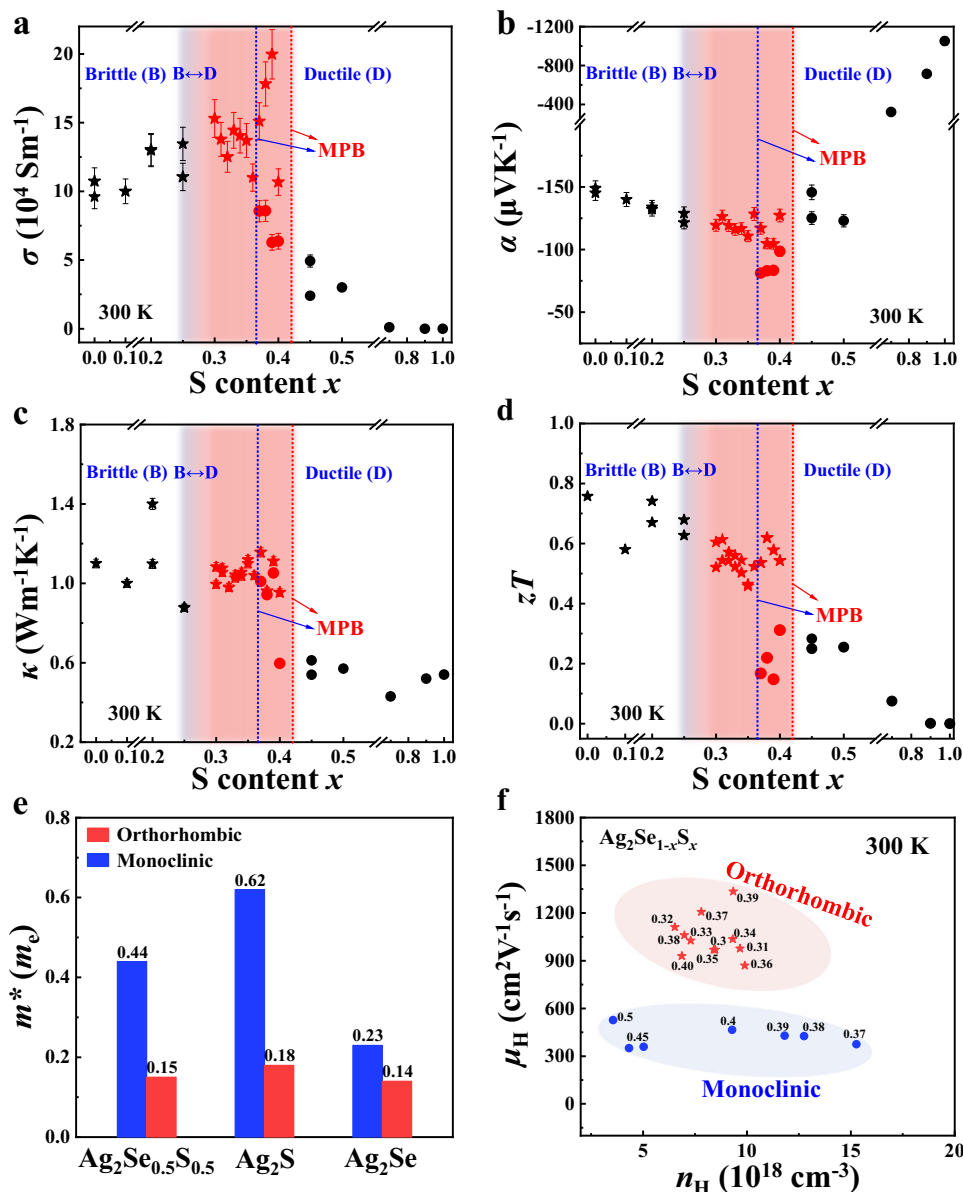
Fig. 3 | TE properties of Ag$_2$Se$_{1-x}$S$_x$ pseudobinary compounds. Room-temperature **a** electrical conductivity (σ), **b** Seebeck coefficient (α), **c** thermal conductivity (κ), and **d** TE figure of merit (zT) as a function of S content. The dashed lines are the MPB in the heating and cooling processes. The error bars in **a**–**c** represent ±9%, ±4%, and ±2%, respectively. **e** Calculated carrier effective mass (m^*) near the conduction band minimum for Ag$_2$Se$_{0.5}$S$_{0.5}$, Ag$_2$S, and Ag$_2$Se crystallized in orthorhombic and monoclinic structures. m^* is defined as the arithmetic mean of the carrier effective mass along the Γ-X, Γ-Y, and Γ-Z directions. **f** Room-temperature Hall carrier mobility (μ_H) as a function of the Hall carrier concentration (n_H) for orthorhombic and monoclinic Ag$_2$Se$_{1-x}$S$_x$.

In summary, we show that the TE performance of ductile materials is pushed to a high value close to that of classic Ag$_2$Se- and Bi$_2$Te$_3$-based materials by modulating the monoclinic–orthorhombic MPBs in Ag$_2$Se-Ag$_2$S pseudobinary phases. The flexible TE devices made from such excellent ductile materials demonstrate the outstanding normalized power density and good service durability of the material. The results of this study indicate that ductile TE materials can realize high output power similar to classic brittle TE materials and thus greatly accelerate the application of flexible TE technology for wearable electronics.

Methods
Sample preparation
Polycrystalline Ag$_2$Se$_{1-x}$S$_x$ pseudobinary compounds were prepared from high-purity sliver shots (99.999%, Alfa Aesar), sulfur bulks (99.999%, Alfa Aesar), and selenium shots (99.999%, Alfa Aesar). The stoichiometric mixtures were weighed, sealed in evacuated quartz

tubes under a pressure of 10^{-4} Torr, placed in a vertical furnace, heated to 1273 K, and placed at this temperature for 12 h. Then, the tubes were slowly cooled to 723 K with a cooling rate of 20 K h^{-1}, dwelled at 723 K for 12 h, and finally cooled to room temperature. The as-prepared ingots were directly cut into specific shapes. Some of the samples were sealed in evacuated quartz tubes, annealed at 473 K for 48 h, and naturally cooled to room temperature. Some of the samples were dipped in liquid nitrogen (78 K) for 48 h and naturally heated to room temperature. These obtained samples were used for the following characterizations.

Sample characterization
The element distribution at the microscale was determined by an energy dispersive spectrometer (EDS; ZEISS® Supra 55). As shown in Fig. S15, all elements were homogeneously distributed inside the prepared Ag$_2$Se$_{1-x}$S$_x$ samples. Furthermore, the EDS mapping
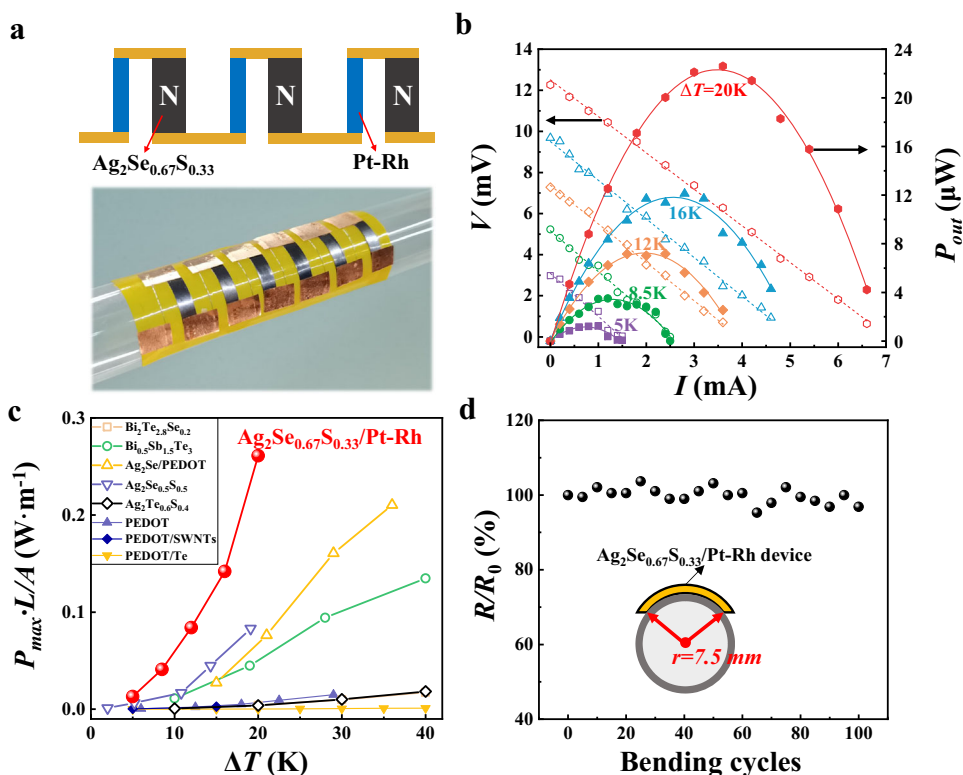
Fig. 4 | Flexible in-plane Ag₂Se₀.₆₇S₀.₃₃/Pt–Rh device. a Sketch map and optical image. **b** Output voltage (V) and power output (P) as a function of current (I) under different operating temperature differences (ΔT = 5 K, 12 K, 16 K, and 20 K). The cold-side temperature is fixed at 296 K. **c** Comparison of the normalized maximum power densities of the materials ($P_{max}L/A$, where P_{max} is the maximum P at each ΔT and L and A are the length and cross-sectional area of the TE legs, respectively)

among the $Ag_2Se_{1-x}S_x$-based inorganic TE devices, inorganic–organic hybrid flexible TE devices, and organic flexible TE devices. The data are taken from Refs. [17,20,51–56]. **d** Relative electrical resistance variation (R/R_O) of the Ag₂Se₀.₆₇S₀.₃₃/Pt–Rh device after bending for different cycles. The inset shows a sketch map of the bending process. The bending radius is 7.5 mm.

characterized by using TEM equipment (TECNAI F20) indicated that the samples had high homogeneity at the nanoscale (Fig. S16). The heat flow curves were measured by differential scanning calorimetry with a heating/cooling rate of 5 K min⁻¹ (Netzsch® DSC 200F3). As shown in Fig. S17a, the different heating/cooling rates (10 K min⁻¹, 5 K min⁻¹, and 1 K min⁻¹) only influenced the intensities of the endothermic/exothermic peaks but scarcely influenced the initial phase transition temperatures. In addition, Fig. S17b shows that the measured heat flow curves had good repeatability. The phase composition and crystal structure were examined by X-ray diffraction (XRD) analysis (D8 ADVANCE instrument, Bruker Co. Ltd). The electrical conductivity (σ) and Seebeck coefficient (α) were simultaneously measured by modified thermal expansion equipment (Netzsch, DIL 402 C). Details about the thermal conductivity (κ) measurements can be found elsewhere[17]. The Hall coefficient (R_H) was measured by the Van der Pauw method (LakeShore® 8400 series) by sweeping the magnetic field from −0.9 T to +0.9 T at 300 K. The Hall carrier concentration (n_H) and Hall mobility (μ_H) were estimated by the relationships $n_H = 1/eR_H$ and $\mu_H = \sigma R_H$, respectively. Bending tests were conducted on a dynamic mechanical analyzer (DMA 850) with a loading rate of 0.05 mm min⁻¹. The specimen dimensions for the bending test were approximately $1.5 \times 0.6 \times 9$ mm³. Compression tests were conducted on an Instrons 5566 universal machine at a loading rate of 0.2 mm min⁻¹. The specimen dimension for the compression test was approximately $3 \times 3 \times 6$ mm³. All specimens were cut directly from the as-prepared ingots.

Device fabrication and tests
The Ag₂Se₀.₆₇S₀.₃₃ materials used for the device fabrication were fabricated by the cooling process. Thin films of Ag₂Se₀.₆₇S₀.₃₃ were

obtained by roller pressing (KJ group, MSK-HRP-1A). The films were sealed in quartz tubes under a pressure of 10⁻⁴ Torr and annealed at 473 K for 48 h. The Ag₂Se₀.₆₇S₀.₃₃ films were cut into long strips with dimensions of $0.1 \times 3 \times 20$ mm³ by scissors as n-type TE legs. Pt-Rh wires with a diameter of 0.2 mm were used as the p-type legs. Copper foils were used as the electrodes. Spot welding was used to connect copper foil with Pt-Rh wires and Ag₂Se₀.₆₇S₀.₃₃ strips. The fabrication details of $(AgCu)_{0.995}Se_{0.25}S_{0.05}Te_{0.7}$ could be found elsewhere[1].

The performance of the TE device was measured using a custombuilt instrument. By adjusting the resistive load in the circuit, the I-V curve was recorded for power output calculations. Under each temperature difference, the maximum power output ($P_{max} = V_{OC}^2/4R_{in}$, wherein R_{in} is the inner resistance of the device) was reached when the resistance of the external electrical load was matched with the internal resistance of the device. A series of temperature differences (5 K, 8.5 K, 12 K, 16 K, and 20 K) was produced by heating one side of the device using a resistance heater, while the cold site was fixed at 296 K.

Calculations
The first-principles calculations were performed based on density functional theory (DFT) as implemented in the VASP program[57]. Projector augmented wave (PAW)[58] potentials were used to describe core–valence interactions, and plane waves reaching a kinetic energy of 350 eV were used as the basis set. The PBE functional[59] was used to optimize the atomic structures and calculate the energy with the DFT-D3 method utilized to describe the van der Waals interactions[60]. The atomic structures of $Ag_2Se_{1-x}S_x$ in both monoclinic and orthorhombic phases were constructed based on the primitive cells of Ag₂S (monoclinic) and Ag₂Se (orthorhombic). The cell and atomic structures were relaxed until the residual forces on all atoms were smaller than 0.01 eV,

and the energy was calculated. The modified Becke–Johnson exchange potential was used in the band structure calculation[61,62] to improve the accuracy of band gap estimation. A $6 \times 4 \times 4$ k-point mesh was used to relax the atomic structure, and a $10 \times 6 \times 6$ k-point mesh was used to calculate the charge density. The effective masses were calculated by fitting the electronic band structure to quadratic functions near the CBM (both are at the Γ point) along the three principal axes.

Data availability

All data are available in the manuscript and in the supplementary materials.

References

1. Yang, Q. et al. Flexible thermoelectrics based on ductile semi-conductors. *Science* **377**, 854–858 (2022).
2. Nan, K. W. et al. Compliant and stretchable thermoelectric coils for energy harvesting in miniature flexible devices. *Sci. Adv.* **4**, eaau5849 (2018).
3. Wang, Y. et al. Flexible thermoelectric materials and generators: challenges and innovations. *Adv. Mater.* **31**, 1807916 (2019).
4. Shi, X. & He, J. Thermopower and harvesting heat. *Science* **371**, 343–344 (2021).
5. He, J. & Tritt, T. M. Advances in thermoelectric materials research: Looking back and moving forward. *Science* **357**, eaak9997 (2017).
6. Tang, X., Li, Z., Liu, W., Zhang, Q. & Uher, C. A comprehensive review on Bi2Te3-based thin films: thermoelectrics and beyond. *Interdiscip. Mater.* **1**, 88–115 (2022).
7. Han, Z. et al. Room-temperature thermoelectric materials: Challenges and a new paradigm. *J. Materiomics* **8**, 427–436 (2022).
8. Yan, Q. & Kanatzidis, M. High-performance thermoelectrics and challenges for practical devices. *Nat. Mater.* **21**, 503–513 (2022).
9. Zhang, J. et al. Discovery of high-performance low-cost n-type Mg3Sb2-based thermoelectric materials with multi-valley conduction bands. *Nat. Commun.* **8**, 13901 (2017).
10. Roychowdhury, S. et al. Enhanced atomic ordering leads to high thermoelectric performance in AgSbTe2. *Science* **371**, 722–727 (2021).
11. Sun, Y. et al. Organic thermoelectric materials and devices based on p- and n-Type Poly(metal 1,1,2,2-ethenetetrathiolate)s. *Adv. Mater.* **24**, 932–937 (2012).
12. Li, J. et al. Polymer-based thermoelectric materials: A review of power factor improving strategies. *J. Materiomics* **8**, 204–220 (2022).
13. Yang, C. et al. A thermally activated and highly miscible dopant for n-type organic thermoelectrics. *Nat. Commun.* **11**, 3292 (2020).
14. Lee, C., Park, Y. H. & Hashimoto, H. Effect of nonstoichiometry on the thermoelectric properties of a Ag2Se alloy prepared by a mechanical alloying process. *J. Appl. Phys.* **101**, 024920 (2007).
15. Kim, S. I. et al. Dense dislocation arrays embedded in grain boundaries for high-performance bulk thermoelectrics. *Science* **348**, 109–114 (2015).
16. Shi, X. et al. Room-temperature ductile inorganic semiconductor. *Nat. Mater.* **17**, 421–426 (2018).
17. Liang, J. et al. Flexible thermoelectrics: from silver chalcogenides to full-inorganic devices. *Energy Environ. Sci.* **12**, 2983–2990 (2019).
18. Wei, T. et al. Exceptional plasticity in the bulk single-crystalline van der Waals semiconductor InSe. *Science* **369**, 542–545 (2020).
19. Yang, S. et al. Ductile Ag20S7Te3 with excellent shape-conformability and high thermoelectric performance. *Adv. Mater.* **33**, 2007681 (2021).
20. He, S. et al. Semiconductor glass with superior flexibility and high room temperature thermoelectric performance. *Sci. Adv.* **6**, eaaz8423 (2020).
21. Hu, H., Wang, Y., Fu, C., Zhao, X. & Zhu, T. Achieving metal-like malleability and ductility in Ag2Te1-xSx inorganic thermoelectric semiconductors with high mobility. *The Innovation* **3**, 100341 (2022).
22. Liang, X. & Chen, C. Ductile inorganic amorphous/crystalline composite Ag4TeS with phonon-glass electron-crystal transport behavior and excellent stability of high thermoelectric performance on plastic deformation. *Acta Mater.* **218**, 117231 (2021).
23. Liang, J., Zhang, X. & Wan, C. From brittle to ductile: A scalable and tailorable all-inorganic semiconductor foil through a rolling process toward flexible thermoelectric modules. *ACS Appl. Mater. Interfaces* **14**, 52017–52024 (2022).
24. Peng, L. et al. Phase-modulated mechanical and thermoelectric properties of Ag2S1-xTex ductile semiconductors. *J. Materiomics* **8**, 656–661 (2022).
25. Liu, J. et al. Enhanced thermoelectric performance in ductile Ag2S-based materials via doping iodine. *Appl. Phys. Lett.* **119**, 6 (2021).
26. Wang, Y., Li, A., Hu, H., Fu, C. & Zhu, T. Reversible room temperature brittle-plastic transition in Ag2Te0.6S0.4 inorganic thermoelectric semiconductor. *Adv. Funct. Mater.* **33** (2023).
27. Wang, Y. et al. Mechanical and thermoelectric properties in Te-rich Ag2(Te,S) meta-phases. *J. Materiomics* https://doi.org/10.1016/j.jmat.2023.08.001 (2023).
28. Wu, H. et al. Optimized thermoelectric performance and plasticity of ductile semiconductor Ag2S0.5Se0.5 via dual-phase engineering. *Adv. Energy Mater.* https://doi.org/10.1002/aenm.202302551 (2023).
29. Ding, J. et al. Selenium-substituted diketopyrrolopyrrole polymer for high-performance p-type organic thermoelectric materials. *Angew. Chem. Int. Edit.* **58**, 18994–18999 (2019).
30. Ju, H. & Kim, J. Chemically exfoliated SnSe nanosheets and their SnSe/Poly(3,4-ethylenedioxythiophene):Poly(styrenesulfonate) composite films for polymer based thermoelectric applications. *ACS Nano* **10**, 5730–5739 (2016).
31. Kim, G.-H., Shao, L., Zhang, K. & Pipe, K. P. Engineered doping of organic semiconductors for enhanced thermoelectric efficiency. *Nat. Mater.* **12**, 719–723 (2013).
32. Lee, S. H. et al. Transparent and flexible organic semiconductor nanofilms with enhanced thermoelectric efficiency. *J. Mater. Chem. A* **2**, 7288–7294 (2014).
33. Lu, Y. et al. Good performance and flexible PEDOT:PSS/Cu2Se nanowire thermoelectric composite films. *ACS Appl. Mater. Interfaces* **11**, 12819–12829 (2019).
34. Qu, S. Y. et al. Highly anisotropic P3HT films with enhanced thermoelectric performance via organic small molecule epitaxy. *NPG Asia Mater.* **8**, e292 (2016).
35. Yao, Q., Wang, Q., Wang, L. M. & Chen, L. D. Abnormally enhanced thermoelectric transport properties of SWNT/PANI hybrid films by the strengthened PANI molecular ordering. *Energy Environ. Sci.* **7**, 3801–3807 (2014).
36. Gao, J. et al. Thermoelectric flexible silver selenide films: compositional and length optimization. *iScience* **23**, 28 (2020).
37. Lu, Y. et al. Ultrahigh power factor and flexible silver selenide-based composite film for thermoelectric devices. *Energy Environ. Sci.* **13**, 1240–1249 (2020).
38. Lu, Y. et al. Correction: Ultrahigh power factor and flexible silver selenide-based composite film for thermoelectric devices. *Energy Environ. Sci.* **13**, 1287–1288 (2020).
39. Jaffe, B., Roth, R. S. & Marzullo, S. Piezoelectric properties of lead zirconate-lead titanate solid-solution ceramics. *J. Appl. Phys.* **25**, 809–810 (1954).
40. Waqar, M., Wu, H., Chen, J., Yao, K. & Wang, J. Evolution from lead-based to lead-free piezoelectrics: Engineering of lattices, domains, boundaries, and defects leading to giant response. *Adv. Mater.* **34**, 2106845 (2022).

41. Liu, Y. et al. Ferroelectric polymers exhibiting behaviour reminiscent of a morphotropic phase boundary. *Nature* **562**, 96–100 (2018).
42. Saito, Y. et al. Lead-free piezoceramics. *Nature* **432**, 84–87 (2004).
43. Li, F. et al. Ultrahigh piezoelectricity in ferroelectric ceramics by design. *Nat Mater* **17**, 349–354 (2018).
44. Liang, J. et al. Crystalline structure-dependent mechanical and thermoelectric performance in $Ag_2S_{1-x}S_x$ system. *Research* **2020**, 6591981 (2020).
45. Pal'yanova, G. A., Chudnenko, K. V. & Zhuravkova, T. V. Thermodynamic properties of solid solutions in the system $Ag_2S–Ag_2Se$. *Thermochimica Acta* **575**, 90–96 (2014).
46. Deng, Y. & Blote, H. W. J. Monte Carlo study of the site-percolation model in two and three dimensions. *Phys. Rev. E* **72**, 016126 (2005).
47. Chen, H. et al. Thermal conductivity during phase transitions. *Adv. Mater.* **31**, 7 (2019).
48. Liu, H. et al. Ultrahigh thermoelectric performance by electron and phonon critical scattering in $Cu_2Se_{1-x}I_x$. *Adv. Mater.* **25**, 6607–6612 (2013).
49. Sun, Y. et al. Flexible n-type high-performance thermoelectric thin films of poly(nickel-ethylenetetrathiolate) prepared by an electrochemical method. *Adv. Mater.* **28**, 3351–3358 (2016).
50. Wang, D. et al. Triggering zT to 0.40 by engineering orientation in one polymeric semiconductor. *Adv. Mater.* **35**, 2208215 (2023).
51. Li, C. et al. A simple thermoelectric device based on inorganic/organic composite thin film for energy harvesting. *Chem. Eng. J.* **320**, 201–210 (2017).
52. Li, Z. et al. A free-standing high-output power density thermoelectric device based on structure-ordered PEDOT:PSS. *Adv. Electron. Mater.* **4**, 1700496 (2018).
53. Lu, Y. et al. Ultrahigh performance PEDOT/Ag_2Se/CuAgSe composite film for wearable thermoelectric power generators. *Mater. Today Phys.* **14**, 100223 (2020).
54. Shang, H. et al. $Bi_{0.5}Sb_{1.5}Te_3$-based films for flexible thermoelectric devices. *J. Mater. Chem. A* **8**, 4552–4561 (2020).
55. Varghese, T. et al. High-performance and flexible thermoelectric films by screen printing solution-processed nanoplate crystals. *Sci. Rep.* **6**, 33135 (2016).
56. Wang, L. et al. Solution-printable fullerene/TiS_2 organic/inorganic hybrids for high-performance flexible n-type thermoelectrics. *Energy Environ. Sci.* **11**, 1307–1317 (2018).
57. Kresse, G. & Furthmuller, J. Efficiency of ab-initio total energy calculations for metals and semiconductors using a plane-wave basis set. *Comp. Mater. Sci.* **6**, 15–50 (1996).
58. Kresse, G. & Joubert, D. From ultrasoft pseudopotentials to the projector augmented-wave method. *Phys. Rev. B* **59**, 1758–1775 (1999).
59. Perdew, J. P. et al. Atoms, molecules, solids, and surfaces: applications of the generalized gradient approximation for exchange and correlation. *Phys. Rev. B* **46**, 6671–6687 (1992).
60. Grimme, S., Antony, J., Ehrlich, S. & Krieg, H. A consistent and accurate ab initio parametrization of density functional dispersion correction (DFT-D) for the 94 elements H-Pu. *J. Chem. Phys.* **132**, 154104 (2010).
61. Becke, A. D. & Johnson, E. R. A simple effective potential for exchange. *J. Chem. Phys.* **124**, 221101 (2006).
62. Tran, F. & Blaha, P. Accurate band gaps of semiconductors and insulators with a semilocal exchange-correlation potential. *Phys. Rev. Lett.* **102**, 226401 (2009).

Author contributions

P.Q. and X.S. designed the study. J.S. L and J.L. prepared the samples and measured the thermoelectric and mechanical properties. J.L. fabricated the devices and measured the output performance. C.M. performed the first-principles calculations. J.S.L., J.L., Z.Z. Z.G. and K.Z. collected the data and provided explanations under the guidance of P.Q., L.C., and X.S. J.S.L., J.L., P.Q., K.Z., L.C., and X.S. wrote and revised the paper. All authors discussed the results and provided helpful suggestions for this work.

Competing interests

The authors declare no competing interests.

Additional information

Supplementary information The online version contains supplementary material available at https://doi.org/10.1038/s41467-023-44318-4.

Correspondence and requests for materials should be addressed to Pengfei Qiu, Kunpeng Zhao or Xun Shi.

Peer review information *Nature Communications* thanks Qingfeng Liu and the other anonymous reviewer(s) for their contribution to the peer review of this work. A peer review file is available.

Reprints and permissions information is available at http://www.nature.com/reprints

Publisher's note Springer Nature remains neutral with regard to jurisdictional claims in published maps and institutional affiliations.